

Defects in Crystals and Crystallographically Challenged Materials

Chapter Outline

9.1. Introduction	372
9.2. Defective Crystals	374
9.2.1. Nanocluster-Enhanced Thermoelectricity in Lead Tellurides	374
9.2.2. A Novel Nanostructure in Gamma Alumina	375
9.2.3. Oxygen ion conductors	377
9.2.4. Intermediate Range Order in Cerium Oxides	378
9.2.5. Defects in Catalytic Support Cerium Oxide, CeO ₂	380
9.2.6. Carbon Nanostructures	386
9.2.7. Earth Science: The Strange Case of Ferrihydrite	393
9.2.8. Earth Science: Biotic Manganese Oxides	394
9.2.9. Structural Response to Metal-Insulator and Magnetic Transitions: Culr ₂ S ₄	396
9.3. Chemical Short-Range Order	397
9.4. <i>In Situ</i> and <i>In Operando</i> Studies	399
9.4.1. <i>In Situ</i> RAPDF Studies of Chemical Reactions Under Flow	399
9.4.2. PDF of an Operating Fuel Cell <i>In Operando</i>	401

9.1. INTRODUCTION

Silicon crystals used in electronics industries are almost perfect, without dislocations and with minimum number of impurities. This is because defects in silicon are electronically charged and interfere with the device operation and industry spends a large amount of money to build special factories to produce these defectless silicon crystals in thin wafers. Except for these cases, all crystals, even precious jewelry crystals, have defects, and these defects often alter or determine their physical properties. Therefore, it is important to characterize these defects, and the PDF method can contribute in some cases if the defect density is high enough. The minimum detectable density of defects varies case by case. The best way to detect them in the PDF is by comparing two samples with and without defects. The difference can be characterized by computing an agreement factor (e.g., see [Chapter 6](#)) between the two experimental PDFs. Experience tells us that, if the density of defects is 10%, they are easy to detect, while if the density is below 1%, it is difficult to become convinced from the PDF that the defects really exist, though the high quality of data from modern sources is pushing this limit down. Why do we bother thinking about the PDF method when there are many other methods to detect defects? In fact, if the nature of the defects is well understood and the only issue is determining their density, the PDF method is not the method of choice. However, if the detailed nature of the defect, such as the local structure within the defect and the lattice relaxation around the defect, is not well known, the PDF method can be an excellent tool. Also when the density of defects is very high, they start to interact with each other and their structure will become modified compared to the isolated state. The PDF method can determine such subtle changes in the local structure with high accuracy.

However, the place where the PDF is having the greatest impact is to find more extensive local disorder in crystalline materials and in studying materials that are so defective that they are on the border between a crystal and a nanocrystal ([Chapter 10](#)) or an amorphous material ([Chapter 12](#)). Examples of such materials are layered materials which are well ordered in the layers or columns but the layers are distorted and disordered ([Fig. 9.1](#)), or a crystal that has a 3D periodic lattice formed by one sublattice of atoms but another sublattice is disordered (e.g., locally correlated broken symmetry phases discussed in [Chapter 8](#)). This is illustrated schematically in [Fig. 9.2](#), taken from the overview article on this topic by [Young and Goodwin \(2011\)](#). There are many more examples that are coming to light as our tools for studying them get better. These materials are also often of great technological interest, precisely for their disorder that imbues special properties, such as for battery electrodes and solid ionic conductors. Many of these studies have been extensively reviewed and we refer readers to these works, for example [Billinge and Kanatzidis \(2004\)](#), [Billinge \(2008\)](#), [Young and Goodwin \(2011\)](#), and last but not least, the first edition of this book. Here, we have replaced many of the

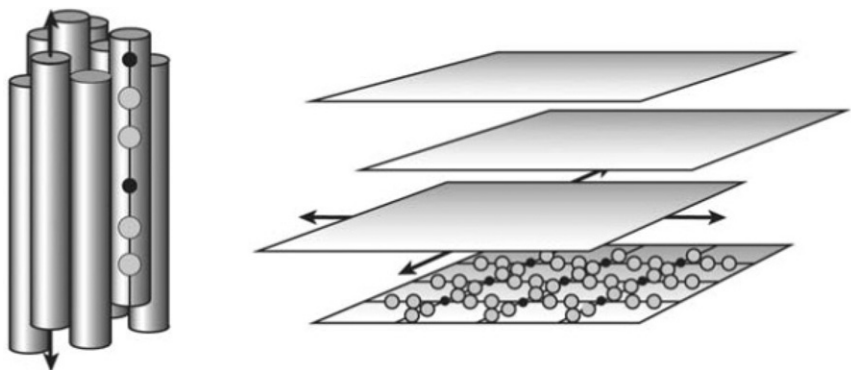


FIGURE 9.1 Schematic diagram of partial order in crystallographically challenged materials. In some cases, the atomic order may be well defined in a layer or a column but poorly defined between the layers and columns (Young and Goodwin, 2011).

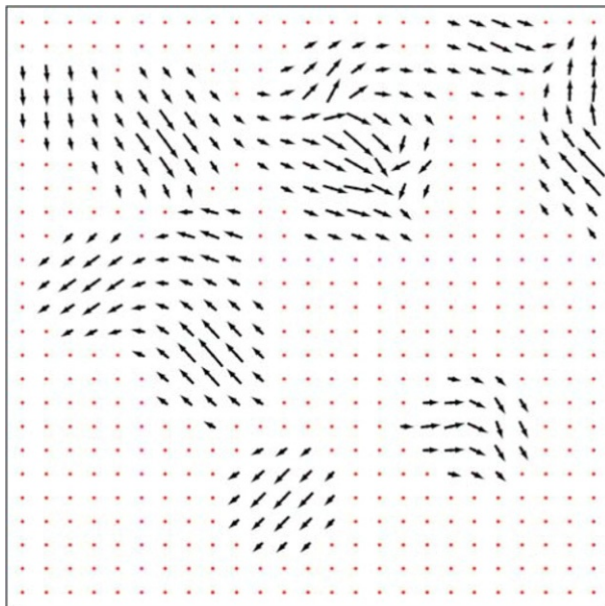


FIGURE 9.2 A symbolic illustration of how locally ordered domains of disorder can exist, either dynamically or statically, in a periodic background coming from a crystal. A study of the Bragg scattering yields information only about the average periodic structure. Total scattering and PDF studies give the average local structure and can see the local atomic displacements (for example) indicated by the arrows (Young and Goodwin, 2011).

examples used in the first book, not because they are not interesting or of current interest but to give us space to highlight some more recent studies. As we have mentioned in the [Preface](#), these are just an appetizer to illustrate the kind of information that can be obtained from a study using total scattering and the PDF. We refer readers to the many studies that are now appearing in the general literature for the main course!

9.2. DEFECTIVE CRYSTALS

9.2.1. Nanocluster-Enhanced Thermoelectricity in Lead Tellurides

Thermoelectricity has great potential for increasing energy efficiency by turning waste heat into electricity and also, run backward, in solid-state refrigeration applications. It relies on the thermoelectric effect such that a temperature gradient across a material results in an electrical voltage. The physics behind it is that hot electrons are moving faster, so they tend to diffuse away from the hot end of the metal and toward the cool end. As this happens, a charge gradient is set up with an associated reverse voltage which tends to drive them back. An equilibrium is established at a certain voltage for a given temperature gradient, depending on the material. To maximize the effect, one wants the electrical conductivity to be high but the thermal conductivity to be low, but these quantities are often positively correlated because the electrons themselves carry heat, so good electrical conductors are good thermal conductors, which is the opposite of what is desired here. The best thermoelectrics turn out to be narrow band-gap semiconductors with low-thermal conductivities, so-called “electron crystals, phonon glasses.” For applications just above room temperature, doped lead telluride is currently the best material. A recent understanding has emerged that the chemical dopants are separating into different composition nanoparticles embedded in the host lattice ([Hsu et al., 2004](#)). The nanoparticles are presumably causing phonon scattering that contributes to the very low thermal conductivity of these materials. PDF was used to characterize these aperiodic defects including composition and structural parameters ([Lin et al., 2005, 2009](#)). However, a surprise emerged when the PbTe endmember was studied on its own. At low temperature, everything was fine; the PDF peaks appeared harmonic and the normal rock-salt fcc structure fit the data well. However, on warming through the temperature range 100–150 K, the PDF peaks became anomalously broad, asymmetric, and non-Gaussian: the structure appeared to become disordered on warming with off-centering Pb displacements, though there was no evidence for this in the crystallography ([Bozin et al., 2010](#)), something that has been termed “Emphanisis,” meaning the emergence of something from nothing. This is illustrated in [Fig. 9.3](#). What appears to be happening is that, although the ground state is undistorted, on warming there is a crossover to a state that resembles a paraelectric state, the state of fluctuating structural

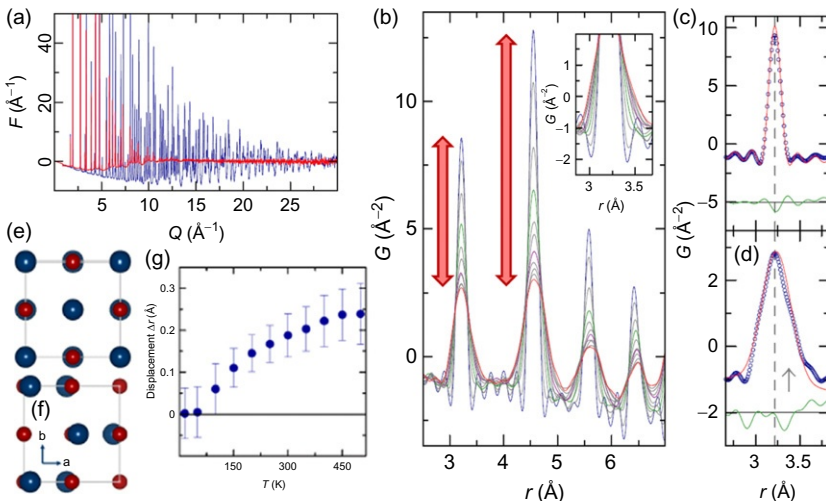


FIGURE 9.3 Evidence for emphanis in PbTe. (a) The crystal structure is very soft. The Debye Waller factor becomes very large with increasing temperature. The blue diffraction pattern is at 15 K and the red at 500 K. (b) This is reflected in the PDF peaks that become very broad and low with increasing temperature, even the first one between directly bonded Pb and Te ions. This is unusual. Near-neighbor peaks in the PDF are often much less temperature dependent than far-neighbor peaks. This peak is emphasized in (c) and (d) where it is clearly becoming asymmetric and non-Gaussian at 500 K in the lower panel. (e) and (f) show the rock-salt (d) and distorted rock-salt (e) structures appropriate for the low- and high-temperature structures of PbTe, respectively. The size of the Pb off-centering distortion is shown in (g) (Bozin *et al.*, 2012).

dipoles that normally exists above the ferroelectric ground state of ordered dipoles. The dipoles appear out of nothing, hence the Emphanitic name. This behavior had not been seen before in PbTe (or any material for that matter) and was hidden from normal crystallographic analyses because the dipoles are not long-range ordered and thus not evident in crystallography. An inelastic neutron study showed that the dipoles are dynamically fluctuating (Jensen *et al.*, 2012). Here the PDF revealed a completely unexpected broken local-symmetry state that was invisible in a conventional structural analysis.

9.2.2. A Novel Nanostructure in Gamma Alumina

Gamma alumina is one of the stable but nonequilibrium crystalline forms of alumina, but it is particularly valued in applications such as in catalysis as a catalytic support. Despite this, its structure remains controversial because material is only available as a 30–50 nm nanodomain powder making quantitative crystallography difficult. This seemed like a good candidate for study

by PDF; however, it was to reveal yet another surprise. The candidate structure models fit quite well to the “long-range” structure in the PDF beyond 10 Å, but fit very poorly to the low- r region below 5 Å (Paglia *et al.*, 2006). This is shown in Fig. 9.4. The challenge in a situation like this is to find a model that not only preserves the good fit to the intermediate range structure but can also fit well to the local structure. The approach used here was to preserve the layers in the boehmite parent structure but to build bridging oxygens between the layers in a chemically reasonable way (kind of like imagining the chemistry of the gamma alumina formation from its boehmite precursor). This resulted in heavily distorted structure in the interlayer region and resulted in a good fit to the low- r region of the PDF that still preserved the intermediate range structure (Paglia *et al.*, 2006). The model, and a projection of the boehmite precursor structure, is shown schematically in Fig. 9.4. The PDF seems to turn up unexpected surprises in many materials that are already of technological importance but, apparently, barely understood.

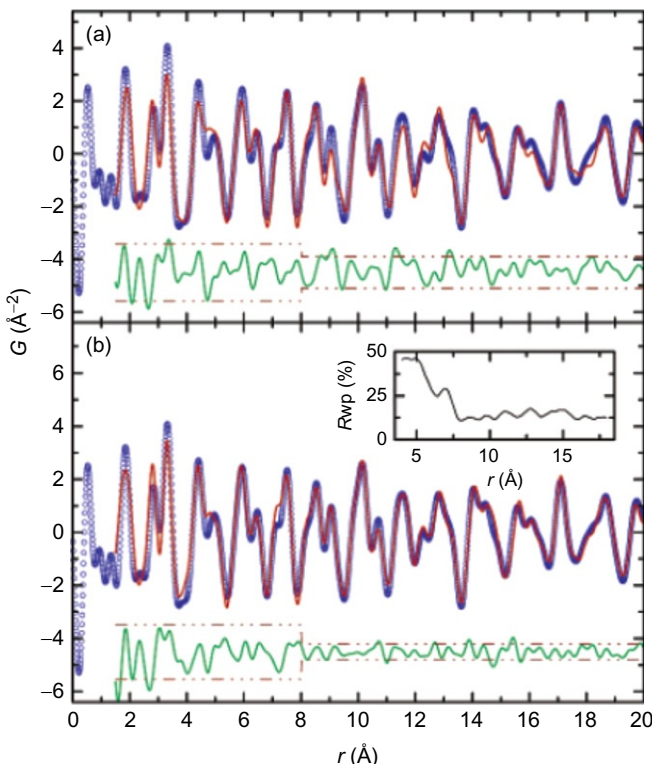


FIGURE 9.4 (a) Experimental PDFs of the gamma alumina (symbols) with PDFs from candidate models from the literature for the structure. The best model (b) fits well above 8 Å, but does a very poor job below that (Paglia *et al.*, 2006).

9.2.3. Oxygen ion conductors

Solid ionic conductors are important as electrolyte materials in fuel cells, for example. They are a classic example of the important role of defects in materials, since the defects are precisely what allow the transport of the oxygen. The mechanism is not well understood. This is a growing area for PDF analysis and a number of studies are emerging. One of the first studied is the phase transition from the nonconducting monoclinic to the highly conducting cubic phase of $\text{La}_2\text{Mo}_2\text{O}_9$ (LAMOX) (Malavasi *et al.*, 2007). The ionic conductivity is thought to be due to the presence of correlated defects on the oxygen sublattice, similar to those seen in other ionic conductors such as the copper halides (Keen, 2002). The phase transition in LAMOX takes place at 580°C and is accompanied by a rather dramatic jump in ionic conductivity. The interesting result from the PDF was that, in the local structure, there is actually no change in the local structure at all at this transition. This is seen quite often, such as the case of BaTiO_3 shown in Fig. 8.5. The LAMOX case is illustrated in Fig. 9.5. The lower panel shows simulations that indicate the change in the PDF that would be expected if the local structure had no disorder and was the same as the crystallographic structure. What is actually seen is in the top panel: there is no change at all in the local structure at this transition. This means that the local structure in the high temperature cubic phase closely resembles the distorted monoclinic local arrangement of atoms seen at

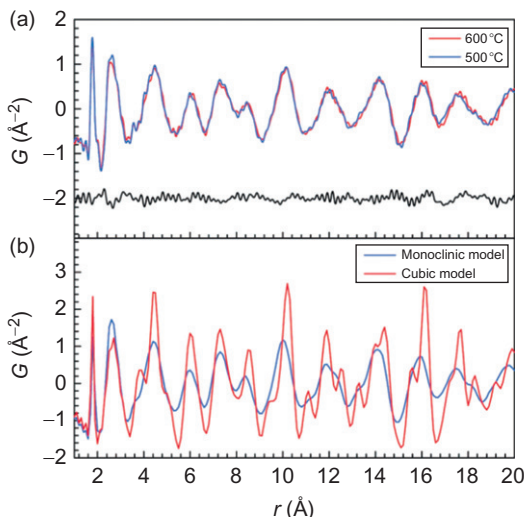


FIGURE 9.5 (a) Actual change in the PDF on going through the monoclinic to cubic phase transition in fast oxygen ion conductor LAMOX. There is virtually no change in the local structure at this transition. (b) expected change in the structure if there was no local disorder in the cubic model (Malavasi *et al.*, 2007).

low temperature. As we discussed in Chapter 3, the PDF gives the instantaneous structure of the material. The long-range monoclinic order of the material is lost but preserved locally. This implies that there are multiple degenerate ways to arrange the monoclinic distortions around the average cubic lattice sites and the structure is breaking up into nanoscale locally monoclinic domains which do not propagate over long range. The dramatic increase in oxygen conductivity implies that the oxygen defects are also becoming mobile, though this is not directly probed by the PDF alone. A similar observation of nanoscale lower-symmetry displacements around a higher symmetry average structure may explain the low thermal conductivity in the thermoelectric material ZnSb (Kim *et al.*, 2007) and is a quite widely observed phenomenon in PDF studies of phase transitions where one often sees modest or no changes in the local structure despite large changes in the global structure.

A more thorough job of modeling the structure of such materials has been carried out on a related fast oxygen conductor based on barium cerate, BaCeO_{2.95} (Malavasi *et al.*, 2009). The local structure in this case shows a significantly distorted environment for the cerium ion compared to the crystallographic prediction which has Ce on a high-symmetry position (Fig. 9.6). Doping just 10% of Y on the cerium site produces significant changes in the PDF, suggesting a larger structural response of the material to the dopant ions. A much lower symmetry model was needed to explain the data (which, *caveat emptor*, may be getting to the point that it is underconstrained and not unique, even from this Small Box modeling approach). However, what is clear is that the higher symmetry crystallographic models are inadequate and the local environment of cerium and oxygen is becoming quite disordered. In the Y-doped case, incorporation of water led to an increase in the local order. The results indicated that a key to understanding the oxygen transport was to have oxygen vacancies that result in rather large local atomic relaxations (Malavasi *et al.*, 2009).

9.2.4. Intermediate Range Order in Cerium Oxides

As we have discussed, high Q -space resolution data result in PDFs that extend higher in r . This is rarely an advantage since PDF modeling is invariably carried out in the very low- r region since we are generally interested in the *local* structure in a PDF study. This explains the success of the RAPDF measurements in many cases since it successfully trades off Q -space resolution for intensity and ease and speed of measurement. However, sometimes the intermediate range information yields important clues about the material properties, as was the case in studies of cerium oxides carried out at the very high Q -resolution ID31 diffractometer at ESRF (M. Brunelli, M. Scavini, C. Oliva, S. Cappelli, private communication, <http://www.science24.com/paper/15339>). In this system, it was desired to see the effects of decreasing particle size on the magnetism in

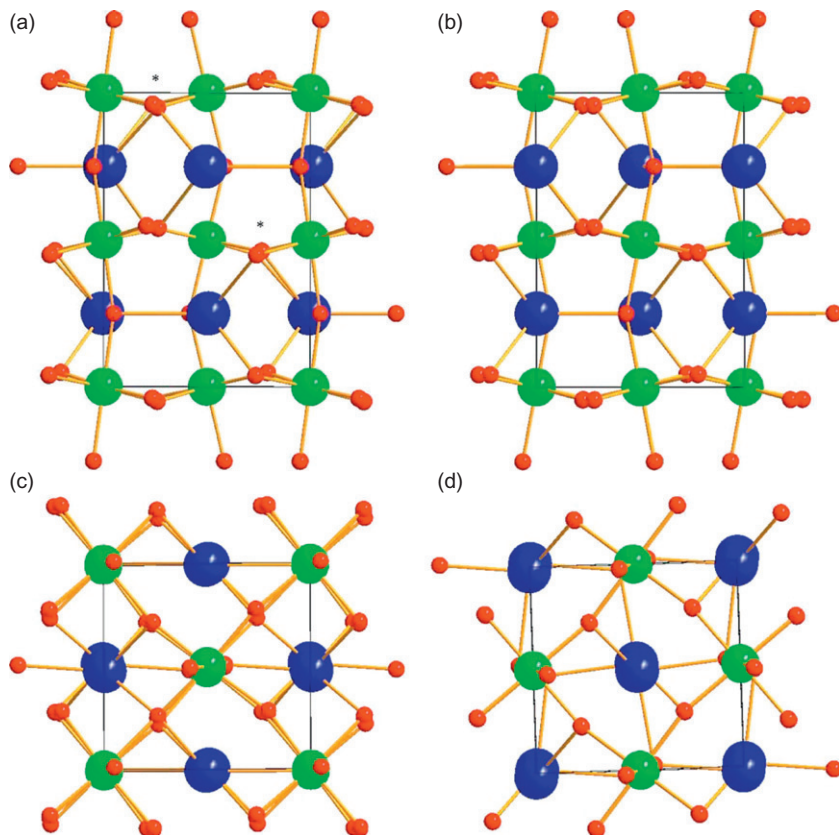


FIGURE 9.6 Schematic figures of the distorted local structures in barium cerate fast oxygen conducting materials. (a) and (c) are from fits to the PDF of yttrium doped $\text{BaY}_{0.1}\text{Ce}_{0.9}\text{O}_{2.95}$ and (b) and (d) from the undoped BaCeO_3 with views down different crystallographic directions (Malavasi *et al.*, 2009).

$\text{Ce}_{0.8}\text{Gd}_{0.2}\text{O}_{1.9}$ particles. The introduction of Gd did not change the local environment of cerium in this case, contrary to the ionic conductors described above, but there were significant changes in the structure on the intermediate length scale, revealed by fitting models over ranges up to 20 nm (200 Å), made possible because of the extremely high Q -resolution of the ID31 data, so that the changes in PDF peak intensities even above 10 nm (> 100 Å) were giving information about the coherence of the structure itself (rather than being due to a loss of coherence of the measurement). This is shown in Fig. 9.7. From these measurements, the PDF of crystalline ceria extends well beyond 100 nm (1000 Å). The “nanoparticles,” which actually are around $10 \times$ larger than those discussed in Chapter 10, decay by around 20 nm.

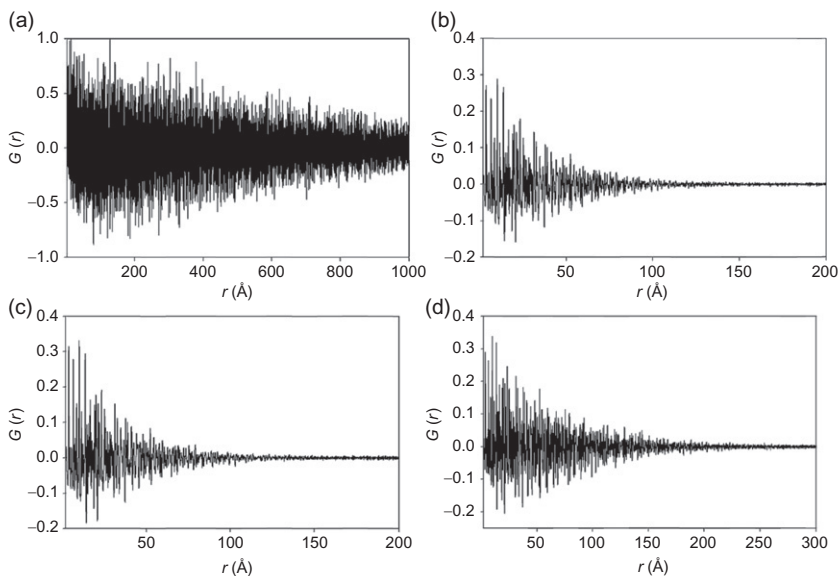


FIGURE 9.7 PDFs from ceria samples from data measured at the high-resolution powder diffraction beamline ID31 at ESRF. (a) bulk ceria. This shows the PDF of the crystalline material which extends to 100 nm or 1000 Å (and beyond). The other panels show different-sized “nanoparticles” (these are much larger than the nanoparticles discussed in this chapter) of gadolinium-doped ceria. Moving clockwise they are nominally 8, 10, and 18 nm diameter (*reproduced with permission by M. Brunelli, M. Scavini, C. Oliva, S. Cappelli, private communication*).

9.2.5. Defects in Catalytic Support Cerium Oxide, CeO_2

Fine particle ceria, CeO_2 , is an important material for the automotive industry. Automotive engine exhaust contains various toxic gases such as CO and NO_x that have to be cleaned by catalytic converters. Thus, the converters have to perform conflicting tasks of reducing NO_x while oxidizing CO and hydrocarbons. By a miracle of modern chemical engineering, small particles of precious metal catalysts such as Pd and Rh can produce simultaneous chemical reactions, such as $\text{NO}_x \rightarrow (1/2)\text{N}_2 + (x/2)\text{O}_2$, $\text{CO} + (1/2)\text{O}_2 \rightarrow \text{CO}_2$, and $\text{CH}_x + \text{O}_2 + (x/4)\text{O}_2 \rightarrow \text{CO}_2 + (x/2)\text{H}_2\text{O}$, on the surface of these particles. However, this is possible only within a narrow specific range of oxygen partial pressure, since O_2 is necessary for oxidation while it makes reduction difficult. The prime role of ceria, CeO_2 , as a catalyst support, is to maintain the local oxygen pressure within this window by releasing or absorbing oxygen through the reaction, $\text{CeO}_2 \leftrightarrow \text{CeO}_{2-x} + (x/2)\text{O}_2$.

One of the major problems with ceria as the catalyst support is an irreversible deterioration of its oxygen storage capacity (OSC) during operation of a catalytic converter. While the old idea was that the loss of surface area due to crystal growth causes this deterioration, it is now well established that the

surface area is not the only important parameter. Various chemical studies suggest that there exist two kinds of oxygen ions, active and inactive. After long use, the active oxygen ions in the ceria are replaced by inactive ones, and ceria loses its capability to store oxygen. However, no microscopic information was available as to what differentiates these two kinds of oxygen ions.

Neutron PDF analysis carried out using the SEPD of IPNS gave the answer to this question ([Mamontov and Egami, 2000](#)). The sample was a 99% pure fine powder of CeO_2 , with grain size of about 70 Å. The data were analyzed both by the Rietveld method and the PDF method. The PDF of ceria powder shown in [Fig. 9.8](#) agrees with the model PDF calculated for the perfect ceria (fluorite) structure reasonably well, but there are significant systematic differences. After extensive Monte Carlo modeling, it was found that the PDF is best explained by introducing interstitial oxygen defects and a balancing amount of oxygen vacancies (Frenkel-type defects) as shown in [Fig. 9.9](#). The agreement factor was reduced from 14.7% (GoF value 2.22) to 9.05% (GoF value 1.37), by introducing 12% of Frenkel defects ([Fig. 9.10](#)). This

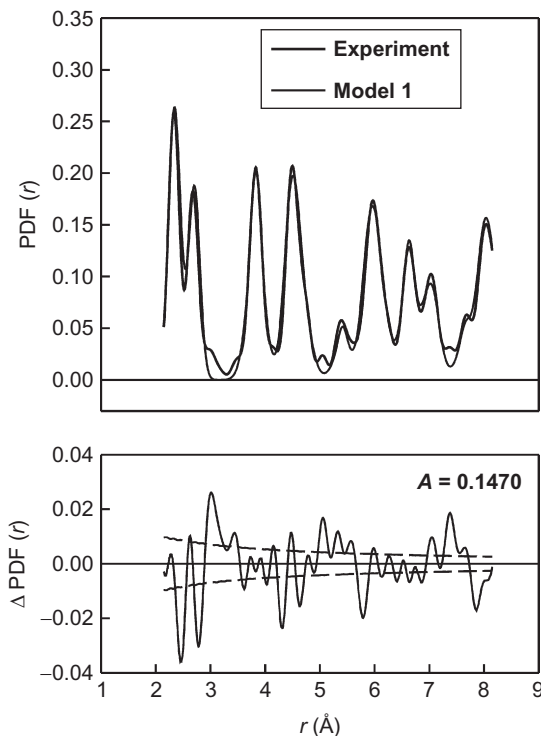


FIGURE 9.8 PDF of nanoparticle ceria, CeO_2 , determined by pulsed neutron scattering (thick line) compared with the PDF calculated for perfect ceria (thin line) and the difference between them ([Mamontov and Egami, 2000](#)).

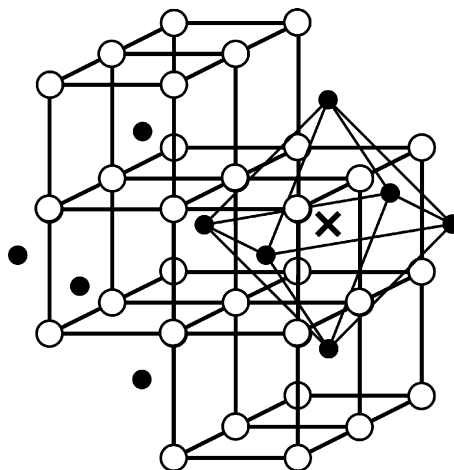


FIGURE 9.9 Interstitial oxygen defects in ceria (Mamontov and Egami, 2000).

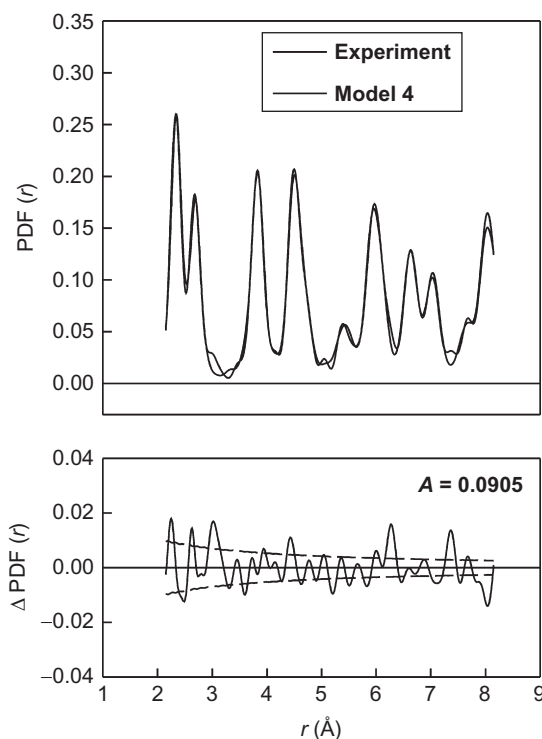


FIGURE 9.10 PDF of nanoparticle ceria, CeO_2 , determined by pulsed neutron scattering (solid line) compared with the PDF calculated for ceria with oxygen defects of Frenkel type (Mamontov and Egami, 2000).

reduction represents a major improvement in fitting. This result was confirmed by Rietveld analysis of the same data as well, after introducing various constraints suggested by the PDF model. Without these constraints, the Rietveld analysis did not converge with the interstitial model. Thus it is highly doubtful if it were possible to discover these defects by the Rietveld method alone. The concentration of the defects refined by the Rietveld method is comparable, about 8%.

The difference between the measured PDF and the model PDF for the perfect structure is plotted also in Fig. 9.8. High-frequency oscillations in the difference PDF are most probably noise, mostly due to the termination error introduced in the Fourier transformation (Section 3.5.2). The wavelength of the high-frequency noise is close to that of the termination error, $7.8/Q_{\max} \sim 0.33 \text{ \AA}$ for $Q_{\max} \sim \text{\AA}^{-1}$. Other errors quickly decrease with r , as discussed before, and are less likely to affect the PDF beyond the range of 2–3 Å. However, the difference PDF has in addition slowly varying components that are not readily caused by the error in $S(Q)$. Furthermore, the differences in the PDF occur only at peaks involving oxygen, and Ce–Ce peaks are well explained by the model PDF. These observations are consistent with the presence of oxygen defects.

An inspection of Fig. 9.8 might lead one to think that the observed PDF may be brought to better agreement with the calculated PDF by subtracting a constant from $g(r)$; one may argue that something went wrong with the normalization of $S(Q)$ so that $g(r) - 1$ is not correctly normalized. As reasonable as it may sound, this argument has a major flaw, which is interesting by itself. First of all, the normalization of $g(r) - 1$ affects tall peaks more than the $g(r) = 0$ line. Since the peaks are in agreement, normalization cannot be much off. Second, it is impossible that some error ends up in adding a constant to the PDF. As discussed in Section 3.1.3.2, $G(r)$ is defined to become zero at large r , and the average density is supplied by hand. So if there is an error, it has to come from the value of ρ_0 . If the value of ρ_0 is reduced, the heights of the PDF peaks also have to be reduced, again resulting in disagreement.

In CeO_2 crystal, Ce ions form an fcc lattice, and O ions occupy the tetrahedral interstitial site of the fcc structure (Fig. 9.9). Remarkably, the octahedral interstitial site is unoccupied in the crystal structure, even though it is more spacious than the tetrahedral site. Since the interstitial oxygens in these octahedral cavities are less strongly bound, they are more likely to come out and facilitate the OSC. Thus, the interstitial oxygen ions are most likely to be the “active” oxygen ions for the OSC.

A direct proof of the annealing effect was obtained by studying the effect of thermal treatment on the ceria sample (Mamontov *et al.*, 2000). As shown in Fig. 9.11, the density of the defects determined by the Rietveld analysis decreased rapidly above 600 °C. At this temperature, also the OSC, determined by the temperature-programmed reduction method, appreciably decreased providing the direct connection between the structural defects and

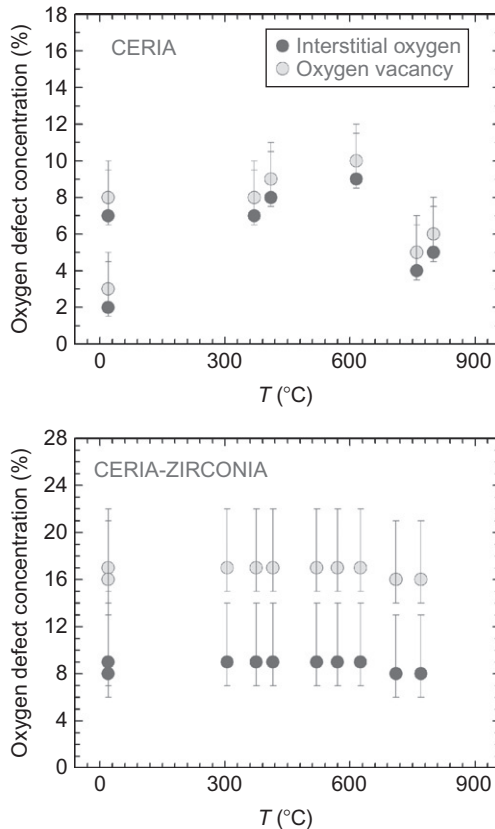


FIGURE 9.11 The density of defects (vacancies and interstitials) as a function of annealing temperature (Mamontov *et al.*, 2000).

the ability of ceria as a catalyst support. While thermal treatment results in the coarsening of crystal grains as well, its temperature dependence does not agree with the change in the defect density and OSC. Thus, it is clear that the reduction in the surface area of powder and thermal diffusion are not the reason for the decrease in the density of defects. The PDFs before and after the heat treatment are compared in Fig. 9.12. The PDF after the treatment is much closer to the model PDF for a perfect structure.

When oxygen ions are reintroduced after reduction, they are likely to occupy the octahedral site first, before they move into the more stable tetrahedral site. Only when the sample is annealed at high temperature, the defects will return to the proper site. This explains why long annealing can deactivate ceria. The nanopowder sample used in this study was prepared by the low temperature ($300\text{ }^{\circ}\text{C}$) calcination of cerium nitrate. Thus, the sample was never exposed to high temperature that would deactivate ceria.

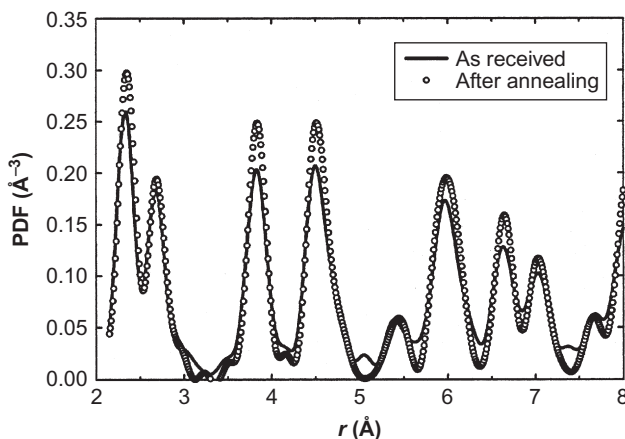


FIGURE 9.12 PDF of ceria before and after thermal treatment (Mamontov *et al.*, 2000).

The figure also shows the concentration of the defects in $(\text{Ce}_{0.8}\text{Zr}_{0.2})\text{O}_2$ as a function of temperature. It is clear that mixing zirconia greatly stabilizes the ceria defects. A possible mechanism of this effect is that alloying zirconia reduces the lattice constant, thus making the tetrahedral site even tighter. This will destabilize oxygen in the tetrahedral site and make it more difficult for the interstitial oxygen in the octahedral site to return to the tetrahedral site.

The interstitial defects, similar to those found in ceria, were observed for the first time in $\text{Ca}(\text{Y})\text{F}_{2+\delta}$ (Cheetham *et al.*, 1971). They have been observed since then in a number of compounds with the fluorite structure. Usually such defects are found in doped systems where the interstitial anions are charge-compensated by cation excess charges. Thermally induced defects of similar type were also observed in pure tetravalent systems (Hutchings *et al.*, 1984). In the latter case, the interstitial anions are charge-compensated by vacancies in the regular anion sublattice.

These results strongly indicate that the oxygen Frenkel-type defects constitute the “active,” weakly bound oxygen observed in the series of recent experiments and define the OSC of ceria in automotive three-way catalytic converters. Thus, the PDF study has identified a very important aspect of the catalyst support oxide. When the density of defects is high enough, greater than a few percent, then the PDF study can be used in identifying and quantifying these defects.

As shown above, mixing zirconia with ceria stabilizes the lattice defects and extends the life of ceria as catalyst support. However, zirconia has additional effects of reinforcing the OSC of ceria. It has been known in the field of catalytic support that a true solid solution of ceria–zirconia is not necessarily the best, but some special processing was needed to produce the best performing ceria–zirconia mixture. The PDF study revealed that the best performing mixture has nanoscale ceria–zirconia segregation within the

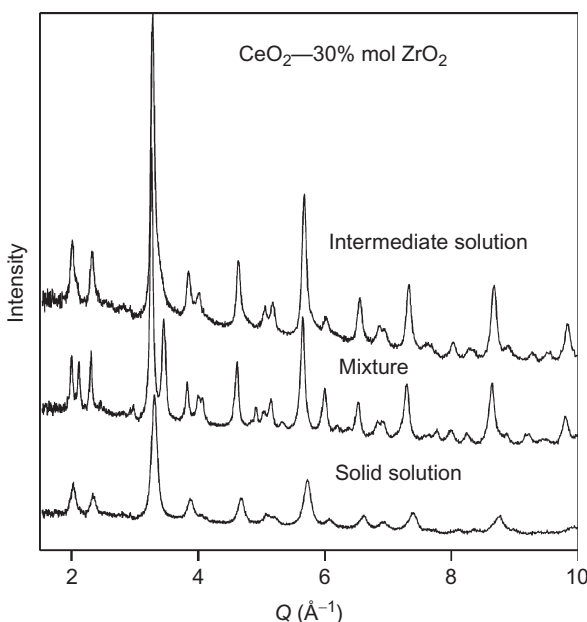


FIGURE 9.13 Diffraction pattern of ceria/zirconia system, in physical mixture, solid solution, and optimal mixture (Egami *et al.*, 1997).

crystalline grain (Egami *et al.*, 1997). While the crystalline size is of the order of 100 Å, the nano-segregation of about 20 Å exists within the grain. As shown in Figs. 9.13 and 9.14, while the diffraction pattern appears to resemble that of a solid solution, the real local structure is closer to the two-phase physical mixture. This was later confirmed by the X-ray small angle scattering. It is conjectured that the nano-segregation helps to create pathways for oxygen. It appears that engineering such nanoscale structure is one of the keys of producing an effective catalyst support.

9.2.6. Carbon Nanostructures

Carbon nanostructures continue to be a very fertile source of new science across several fields including, for example, electron transport and nanoscale electronics (Dresselhaus *et al.*, 1996; Saito *et al.*, 1998). The recent discovery of the amazing properties of grapheme, and the subsequent 2010 Nobel Prize for Andre Geim, Konstantin Novoselov, has only refueled interest in this material (Zhang *et al.*, 2005; Geim and Novoselov, 2007), coming at the heels of 1996 Nobel prize to Robert Curl, Harold Kroto, and Richard Smalley for discovery of fullerenes, C₆₀. Structures range from the simple and intuitive, such as graphite and the C₆₀ molecule, to the complex and highly disordered.

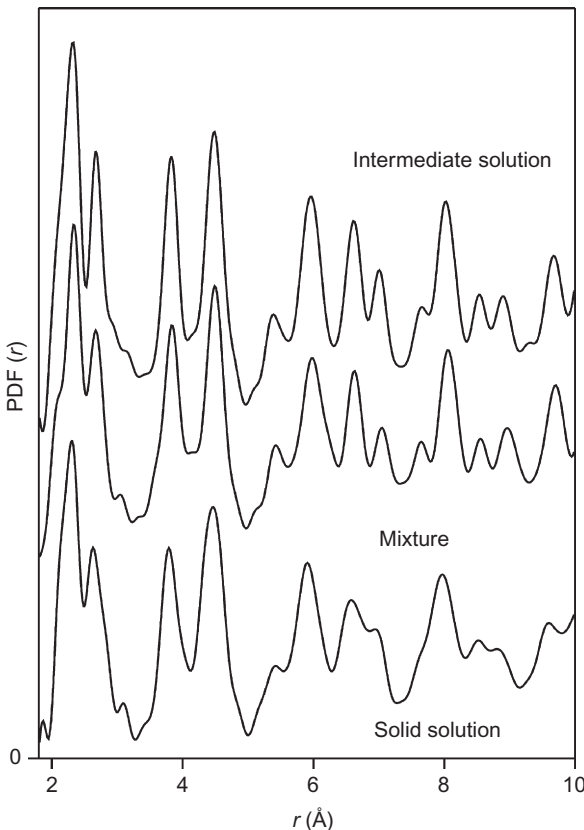


FIGURE 9.14 Pulsed neutron PDF of ceria/zirconia system, in physical mixture, solid solution, and optimal mixture (Egami *et al.*, 1997).

The complex disordered structures have nanoporous properties, but details of the structure are hard to determine.

Even relatively simple solid C_{60} contains disorder since the C_{60} balls sit on high-symmetry special positions in the lattice. The point symmetry of the balls themselves is lower than the point symmetry of the crystallographic site they sit on. This means *a priori* that the internal structure of the balls themselves cannot be solved from the Bragg scattering alone. In fact, in solid C_{60} , considerable diffuse scattering exists that can be straightforwardly analyzed to extract information about the ball structure (Fig. 9.15). At room temperature, the balls are spinning at a fairly high rate. To a good approximation, the structure can be modeled as being made up of isotropic balls making a close-packed fcc lattice (David *et al.*, 1991; Heiney *et al.*, 1991) and below 260 K the balls freeze into a partially ordered arrangement where there is a tendency for the CC double bonds on one molecule to align with the centers of pentagonal faces on the neighboring ball (David *et al.*, 1991; Hu *et al.*, 1992).

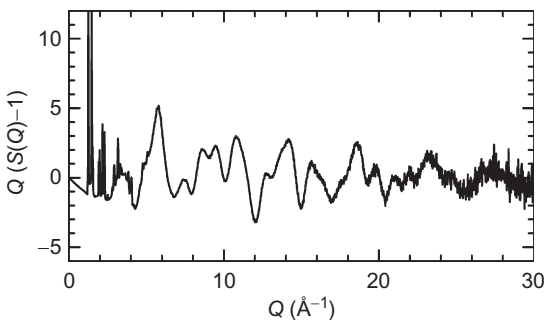


FIGURE 9.15 Reduced structure function from C_{60} from neutron data collected at room temperature. The Bragg peaks from which the fcc structure of C_{60} solid was solved are evident at low Q . The significant diffuse scattering comes from the internal structure of the C_{60} molecule itself.

As we described in Chapter 1, C_{60} provides an excellent example of the importance of studying total scattering (Bragg and diffuse scattering) when analyzing complex solids. The large amounts of diffuse scattering are evident in Fig. 9.20. The resulting PDF is shown in Fig. 9.16 with sharp peaks at low r coming from the balls themselves and broad peaks at higher- r from the ball-ball correlations. The total scattering data can be studied in real space (Li *et al.*, 1991; Hu *et al.*, 1992; Soper *et al.*, 1992; Thorpe *et al.*, 2002) or directly in reciprocal space (David *et al.*, 1991; Copley *et al.*, 1992; Leclercq *et al.*, 1993; Damay and Leclercq, 1994), but in either case, both the Bragg and diffuse scattering must be analyzed. Both neutron and X-ray single crystal diffuse scattering has also been measured from C_{60} and summarized in Pintschovius (1998) and Nield and Keen (2001), and as we showed in Chapter 6, these PDF data of C_{60} data were used to demonstrate the first *ab initio* structure solution of a nanoparticle from PDF data (Juhas *et al.*, 2006).

The study of disordered carbons has a structural scientific pedigree of the highest order, being studied first by Warren (1934) and later by Rosalind Franklin (1950, 1951) whose role in the discovery of the structure of DNA we referred to in Chapter 3. The work of Warren was on porous “Carbon blacks” and an example of one of the first PDF analyses of powder data. The study revealed that the materials were made up principally of graphene sheet fragments. The tedious procedure of Fourier-transforming data, ca. 1934, prompted Warren to come up with the alternative approach for analyzing data from disordered 2D structures such as these directly in Q -space. Scattering from 2D sheets gives rise to a characteristic asymmetric line-shapes for the Bragg lines in powder patterns, with a sharp rise and a long tail on the high-angle side, the now called “Warren line-shape” (Warren, 1941). The data analysis in these early studies was hampered by lack of modern high-flux sources and linear, high-count-rate detectors, and no computing. Nonetheless, the amount of information extracted from the scattering is extraordinary. For

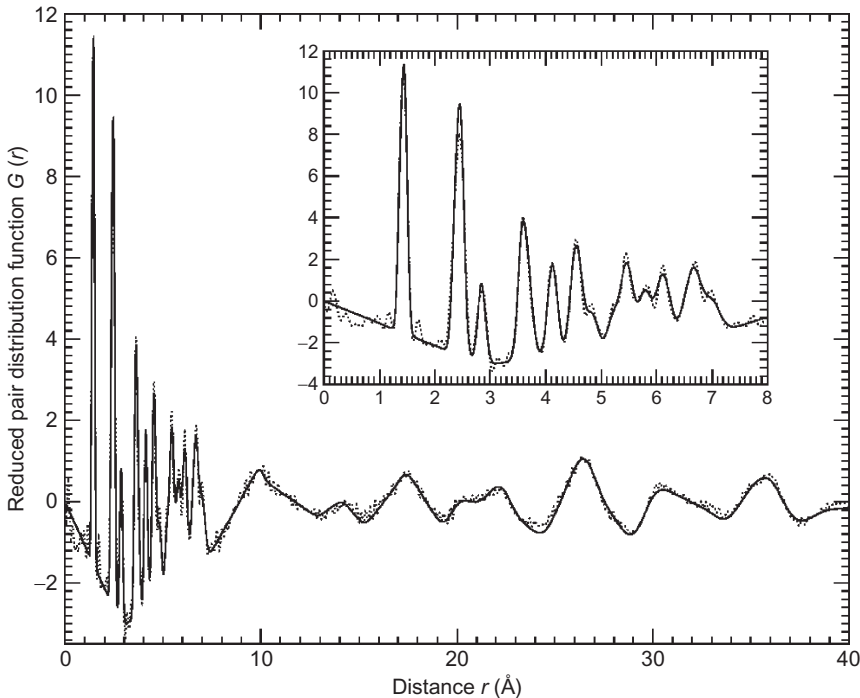


FIGURE 9.16 PDF, $G(r)$, from the data shown in Fig. 9.11 5 (dots) with the calculated structure of C_{60} superimposed. Contrary to the case with the Q -space scattering, the sharp peaks at low r come from the C–C correlations on the C_{60} balls themselves and the broad structure at higher r comes from the fcc arrangement of isotropic hollow balls due to the fact the balls are spinning (Thorpe *et al.*, 2002).

example, in the Franklin (1950) study of pyrolyzed polyvinelidene chloride, which forms a particularly disordered carbon, the structure was determined to be made up of fragments of graphene sheets of $16(\pm 1)\text{ \AA}$ stacked together with a layer spacing of 3.70 \AA (compared to 3.35 \AA for pure graphite); that 65% of the carbon is in the form of graphene sheet fragments, of which 55% is stacked with two or more layers parallel; and that the fragments approach each other to a separation of 25 \AA . A more complete study of a series of carbons with differing degrees of disorder resulted in a view of the structure of graphitizing and nongraphitizing carbons as shown in Fig. 9.17. The picture that emerged in 1950 has a remarkable similarity to that obtained in 1999 using advanced computer modeling (Acharya *et al.*, 1999) and from the much wider Q -range neutron data shown in Fig. 8.24b (Petkov *et al.*, 1999; Fig. 9.18). The quality in the low- Q region of the 1950 and 1999 data-sets can be compared in Fig. 9.19a and b (note that, to convert the x -axis of the Franklin (1950) data to the same units as the Petkov *et al.* (1999) data,

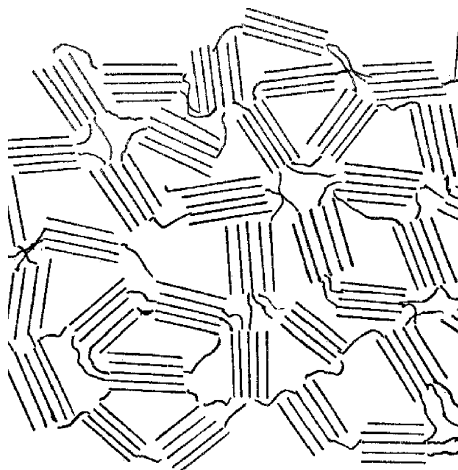


FIGURE 9.17 Model for highly disordered nanoporous carbon ca. 1950 ([Franklin, 1951](#)).

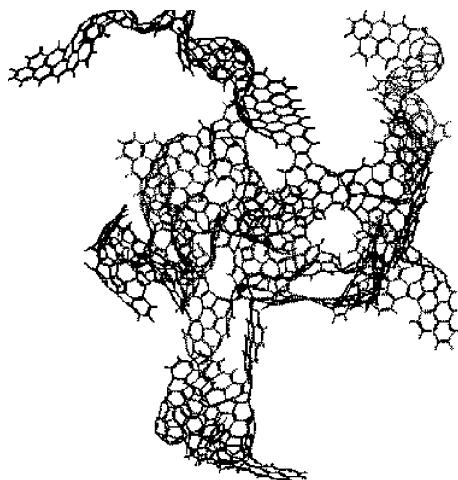


FIGURE 9.18 Model for highly disordered nanoporous carbon ca. 1999 ([Acharya *et al.*, 1999](#)).

it should be multiplied by 2π). The main difference between the datasets clearly comes from the range of Q now accessible, and this is evident as much higher real-space resolution in the modern PDF shown in Fig. 9.20c. Note that the original PDF of Franklin had terrible contamination from termination ripples (e.g., see the spurious ripple at $r = 1.9 \text{ \AA}$ in Fig. 9.20a) that were eliminated by damping the data, as discussed in Section 5.3.10 and resulting in the PDF in Fig. 9.20b. In the 1999 study, the termination ripples in $G(r)$ are minimal without any data damping (Fig. 9.25c), illustrating the importance of measuring data over a wide range of Q . For example, compare the second

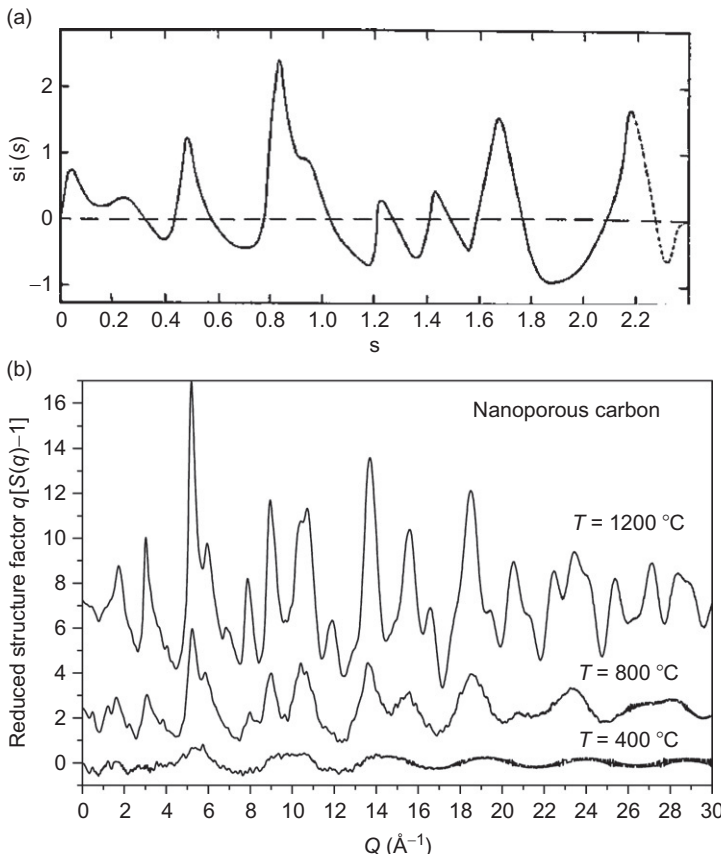


FIGURE 9.19 (a) Structure function from pyrolyzed polyvinelidene chloride measured in 1950 using laboratory X-rays by Franklin (1950). (b) Structure functions from pyrolyzed polyfurfuryl alcohol, with the pyrolyzation temperature shown, measured using spallation neutrons in 1999 (Petkov *et al.*, 1999). Both show the same representation of the data ($Q[S(Q)-1]$) but the scale in (a) should be multiplied by 2π to compare it with the data in (b). The Q -range of the 1950 data is therefore $0 < Q < 15 \text{\AA}^{-1}$.

and third C–C peaks between 2 and 3 Å in Fig. 9.20c. These are completely resolved in Fig. 9.20c, completely unresolved in Fig. 9.20b, and evident as a shoulder (but smaller than the termination ripple at 1.9 Å) in Fig. 9.20a. The need to collect high-quality data over a wide Q -range cannot be overemphasized.

We now understand that the graphene sheets can be significantly bent by introducing pentagons and this contributes to the loss of structural coherence as well as sheet fragmentation (Fig. 9.18). In the more disordered carbons, the sheets also can support defects that preserve the network such as higher-membered rings (seven and eight, for example). This is apparent because with

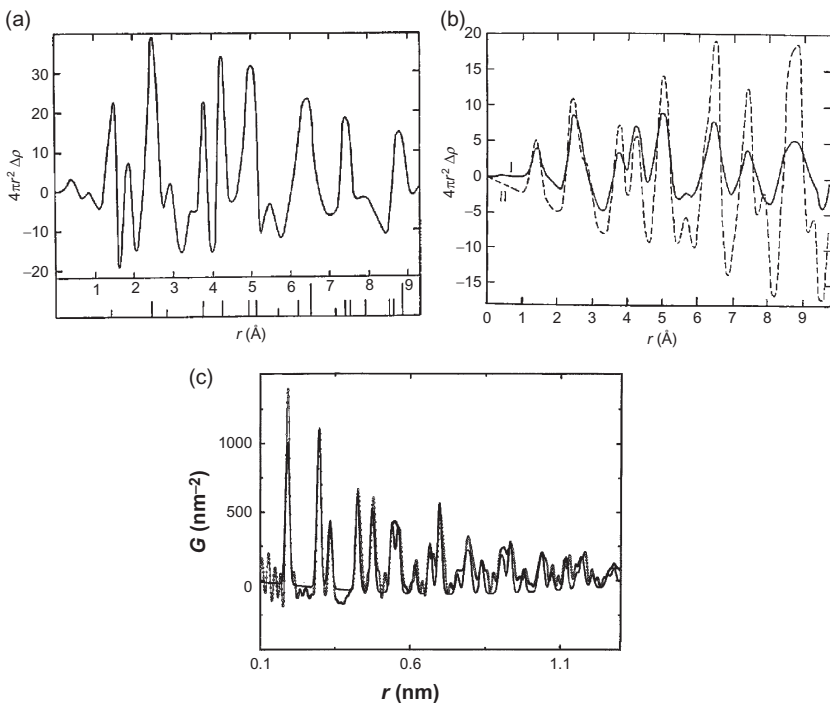


FIGURE 9.20 (a) PDF of nanoporous carbon from the data shown in Fig. 9.19a. (b) (solid line) PDF from the same data after damping the data to minimize termination ripples. Note the spurious ripple at $r = 1.9$ Å in (a) has disappeared after damping the data (b), but the PDF has become significantly broadened. The dashed line shows the PDF calculated for graphite (Franklin, 1951). (c) PDF from the modern spallation neutron data shown in Fig. 9.19b. This PDF was obtained by direct transform (as were the PDFs in panels (a) and (b)) but without damping. The PDF peaks are sharp, the data high resolution, but the spurious termination ripples are minimal. The amplitude of the data falls off quickly with increasing r because of the nanoscale crystallites (Kane *et al.*, 1996).

the higher resolution allowed by a much higher Q_{\max} from modern sources, the second and third neighbor carbon peaks can be resolved (Fig. 9.20c; Petkov *et al.*, 1999) where they could not in the Franklin (1950) data (Fig. 9.20b). Intensity is lost out of the third peak in the more disordered carbons indicating the presence of higher-membered rings.

The structure of pyrolytic carbon remains of interest in the second decade of the twenty-first century (and beyond, undoubtedly) (Weisbecker *et al.*, 2012). Pyrocarbons can be categorized into rough laminar and smooth laminar families that have different porosity and properties. A neutron PDF study using the ID4 diffractometer at ILL (Weisbecker *et al.*, 2012) was used to differentiate structurally between these families for the first time. As shown in Fig. 9.21, the materials are similar in the low- r region but show significant

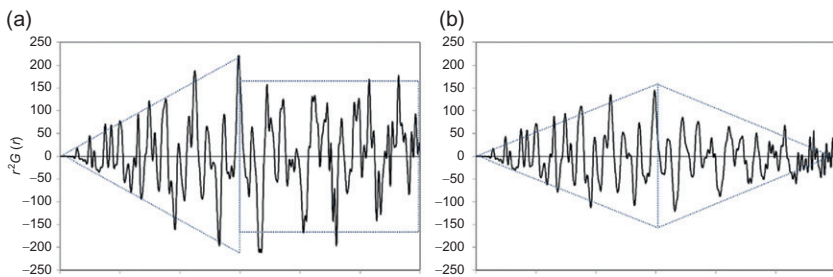


FIGURE 9.21 r^2 -Scaled PDFs from rough laminar (a) and smooth laminar (b) carbon, as determined from property measurements ([Weisbecker et al., 2012](#)).

differences in structural coherence on the intermediate length scale above 15 Å. $G(r)$ curves that have been scaled by r^2 have a very different r dependence from the two classes of carbon material in this region, as shown in the figure. [Weisbecker et al. \(2012\)](#) also describes modeling of the PDF data by extending an image reconstruction guided method based on TEM images ([Leyssale et al., 2009](#)).

Remarkably, in 2012, 62 years after the Franklin work and 78 years after Warren's pioneering work, we are still struggling to understand the structure of these disordered carbons, which, nonetheless, retain their technological and scientific interest ([Dmowski et al., 2012](#)).

9.2.7. Earth Science: The Strange Case of Ferrihydrite

Ferrihydrite is one of the most important and most heavily studied minerals ([Michel et al., 2007](#)). It exists naturally in near-surface strata and is present in pristine soils, but it is nanocrystalline, has a high surface area, and is very reactive and so finds industrial applications in coal liquification and metallurgical process and is found in the highly polluting acid mine drainage. Because of its nanocrystallinity, its structure is highly controversial. It seems as if it is a good candidate for a PDF study as was first carried out by [Michel et al. \(2007\)](#). A structural model was developed through trial and error based on a starting model from the mineral akdalaite. This is an arduous process and it is quite an accomplishment to find a model that gives such a good fit to the data over such a wide range and this was seen as a breakthrough. The fits and a schematic of the model are shown in Fig. 9.22. However, the structure remains controversial. In response to criticism ([Rancourt and Meunier, 2008](#); [Hiemstra and van Riemsdijk, 2009](#); [Manceau, 2009](#)), the same authors proposed an updated model in 2010 ([Michel et al., 2010](#)). In a critique by [Manceau \(2010\)](#), it was pointed out that the models proposed from the PDF study were inconsistent with an earlier model based on X-ray diffraction ([Drits et al., 1993](#)) and on electron nanodiffraction ([Janney et al., 2000](#)) and indeed that the PDF structural models violated a number of Paulings rules

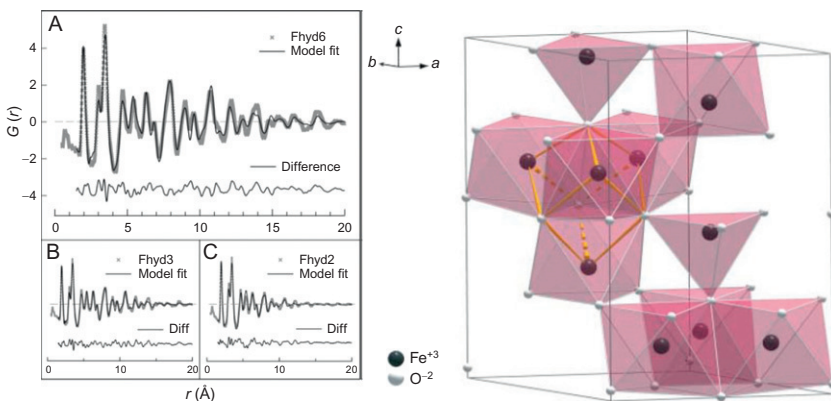


FIGURE 9.22 (left) PDFs measured from ferrihydrite using high-energy X-rays. Solid line is the PDF calculated from the structural model proposed by Michel *et al.* (2007) which is shown on the right (Michel *et al.*, 2007).

and could not possibly be correct. The authors of the PDF studies have also mounted a spirited defense of their models, and at the time of writing, the controversy remains. This may be a case where the PDF data alone cannot constrain a unique solution to the inverse problem, though this remains to be established, and the structure of ferrihydrite is still not satisfactorily solved. There are many more very interesting examples of highly disordered materials from the world of geology and earth science. It turns out that many minerals are actually nanostructured, and it is expected that, despite its difficult start, the PDF method will have a significant impact in this field moving forward.

9.2.8. Earth Science: Biotic Manganese Oxides

Like ferrihydrite, manganese oxides play an important role in earth science (e.g., in biogeochemical elemental cycling, carbon cycling, nutrient speciation, and mediating toxicity of metalloids such as arsenic in the environment) but are also valued in industrial applications for their interesting properties, for example, as battery electrode materials (Zhu *et al.*, 2012). Also, like ferrihydrite, they are nanocrystalline and difficult to characterize crystallographically, for example, the mineral vernadite. This is a material that also highlights another common problem facing structural scientists in earth science; it is heterogeneous and multiphase at the nanoscale. Furthermore, vernadite exemplifies another interesting phenomenon in mineralogy. Its formation is actually catalyzed by microorganisms (e.g., *Bacillus* sp. SG-1, *Pseudomonas putida* MnB1/GB-1, and *Leptothrix discophora* SP-6) in oceanic and terrestrial environments and is an example of a “biogenic” Mn oxide (BioMnO_x): it is a naturally occurring nanocrystalline material made by bugs.

The resulting structure may depend on the bug, for example, bacteria preferring layered MnO_x structures and fungi preferring tunnel structures (Zhu *et al.*, 2010, 2012), or on the bug's environment, for example, the same bacterium producing two different structures depending on whether it was living in solid agar or in an aqueous environment (Grangeon *et al.*, 2009). Clearly a large amount of work remains to be done in the area of structure studies of biogenic minerals, not least because these bugs are producing potentially extremely interesting materials from a technological point of view. This area is hardly exploited from a PDF perspective at present, but what has been done looks promising (Petkov *et al.*, 2009). Samples of biotic MnO_x made by bacteria and fungi were measured using X-ray PDF, as shown in Fig. 9.23 (Petkov *et al.*, 2009). The measured PDFs, and thus the underlying structures, from the two samples are clearly quite different from each other. Plotted on top, and illustrating the arduous trial and error approach of the modeling at present, are plots of fits to the data from a number of trial models coming from different known minerals. In this way, the basic local structural configuration can be elucidated (or at least, incorrect local structural motifs ruled out).

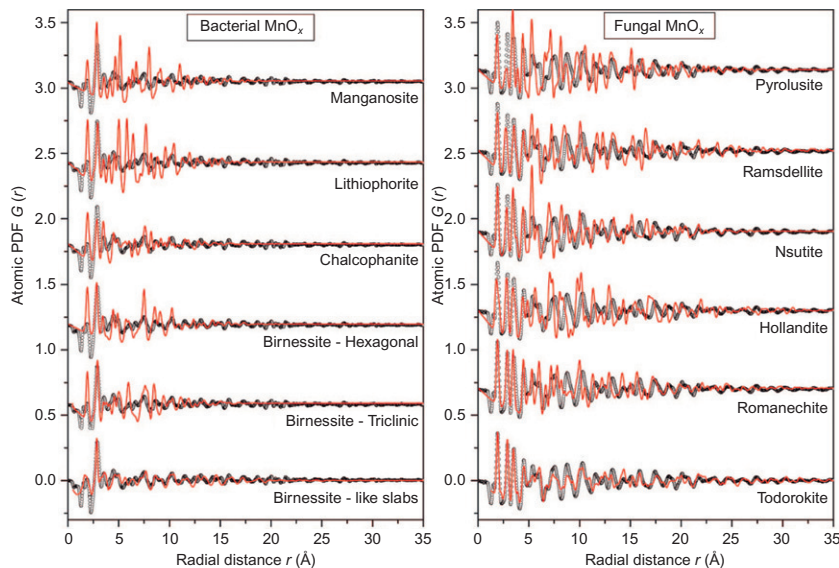


FIGURE 9.23 Comparison of X-ray PDFs from biotic MnO_x samples. The PDFs are from samples made by bacteria (left) and fungi (right). The PDFs, and therefore the structures of the biotic MnO_x materials, are clearly quite different. The solid lines are fits of different structural models in an attempt to find the nature of the structure of the materials (Petkov *et al.*, 2009).

9.2.9. Structural Response to Metal-Insulator and Magnetic Transitions: CuIr₂S₄

As discussed in greater detail in [Chapter 8](#), materials undergoing structural phase transitions are especially suitable for study by PDF methods because the fluctuations into the lower-symmetry phase can be studied even when they are not long-range ordered. A number of materials have electronic or magnetic phase transitions that are not associated with an obvious structural transition. One clear example is cubic perovskite manganites that show colossal magnetoresistance. These materials have a large local structural response to the electronic transition, even when no change in symmetry is seen in the average structure ([Billinge *et al.*, 1996](#); [Bozin *et al.*, 2007](#); [Sartbaeva *et al.*, 2007](#)).

A particularly interesting example of this class of material is CuIr₂S₄. This material is insulating at low temperature, but on warming, it goes through an insulator-metal (IM) transition to a metallic state. At low temperature, it is diamagnetic, losing the significant magnetic susceptibility it has at high temperature. In this case, there is a structural transition and Ir⁴⁺-Ir⁴⁺ chains in the structure are seen to dimerize, moving closer to each other by a massive 0.5 Å ([Radaelli *et al.*, 2002](#)). The transition is understood first as a charge disproportionation from a charge delocalized metallic Ir^{3.5+} state to a charge localized, disproportionated, state of Ir³⁺ and Ir⁴⁺ ions. These arrange in pairs in the structure forming 3+–3+–4+–4+–3+–3+ chains. At the same time, the Ir⁴⁺ dimerize, forming spin singlets and destroying the spin susceptibility and the conductivity of the material. The dimers are clearly seen crystallographically, but they are also easy to see directly in the PDF as a small peak at 3 Å ([Fig. 9.30](#), right panels, indicated by an arrow). The conductivity in the metallic phase is poor, and it was suggested that the IM transition involved the melting of the dimer lattice and mobility of localized charges. The PDF measures the local structure and shows directly whether or not the dimers persist in the metallic phase, even when they are not long-range ordered and therefore invisible crystallographically. It is thus possible using PDF to study the nature of the metallic phase directly. This was done in the study by [Božin *et al.* \(2011\)](#) by crossing the IM boundary using different methods: by heating, by irradiation by intense X-rays, and by doping with Cr. The PDFs of the material straddling the transition line are shown in [Fig. 9.24](#). In the top and the bottom panel, the IM transition is crossed by heating and by Cr doping, respectively. For comparison, in the middle panel, the transition is not crossed, but the two PDFs are separated by the same temperature interval as those in the top panel. This shows the reproducibility of the data and the size of the changes due just to thermal effects. It is clear that there is a large local structural response to the IM transition as evidenced by the large-scale fluctuations in the difference curve in the top and bottom panels. It shows that the IM transition is accompanied by the destruction of the dimers when it is crossed as a function of temperature and Cr doping.

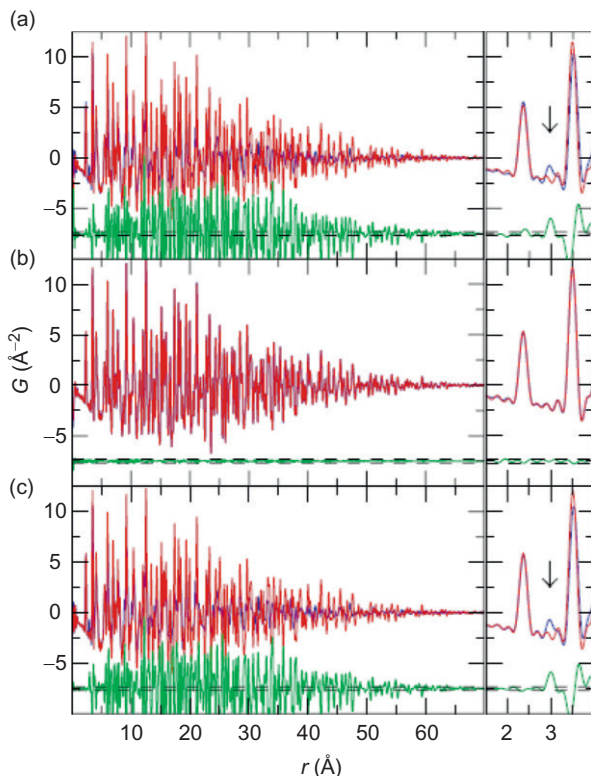


FIGURE 9.24 PDFs from CuIr_2S_4 . In each panel, two PDFs are compared with a difference curve offset below. On the right, the same two PDFs are plotted to emphasize the low- r region of the PDF and to show the appearance of the PDF peak at 3 \AA from the $\text{Ir}^{4+}-\text{Ir}^{4+}$ dimer. In (a) and (c), the PDFs shown straddle the IM phase transition line. In (a), the transition is crossed by warming and in (c) by doping Cr. (b) shows the changes expected due to thermal effects where the two PDFs are separated in temperature by the same amount as those in (a), but they do not straddle a phase line. There is clearly a large change in local structure at the IM transition and the dimers are destroyed right at the transition (Božin *et al.*, 2011).

Interestingly, the same was not true when the material was driven metallic by exposure to intense X-rays. This is very direct, model-independent, evidence in the PDF that gives crucial information to help understand these interesting and unusual phase transitions.

9.3. CHEMICAL SHORT-RANGE ORDER

Most PDF studies on crystals to date have concentrated on extracting information about atomic disorder, in the form of atom displacements from their

average positions, and indeed the PDF is most sensitive to this. However, information is contained in the PDF about chemical ordering. Chemical long-range order results in superlattice Bragg peaks, for example, as extensively studied in chemical order-disorder transitions such as in Cu₃Au (e.g., see Cowley, 1995). As with the case of disordered carbon, the list of people who have worked on order-disorder phenomena in alloys has a scattering “hall of fame” ring to it, including Warren, Cowley, Shockley, Lipson, Guinier, Krivoglaz, and Moss (Krivoglaz, 1969, 1996; Warren, 1990; Cowley, 1995). Above the ordering transition, short-range ordering of the chemical species persists and can be studied using diffuse scattering (Cowley, 1950; Moss, 1964). This is still today a topic of great interest in nonstoichiometric compounds such as doped semiconductors, semiconductor alloys, and oxides such as high- T_c cuprates where chemical short-range order (CSRO) can significantly modify the properties. It is interesting to know whether this information can be extracted from the PDF and this has been investigated recently (Proffen, 2000; Proffen *et al.*, 2002). In this study, data were first simulated and the CSRO information was extracted successfully from the simulated data using a reverse Monte Carlo approach (Proffen, 2000).

This has also been successfully demonstrated in real data from the Cu₃Au system (Proffen *et al.*, 2002). In this case, X-ray PDFs from fully ordered Cu₃Au, and a disordered compound quenched from high temperature, were compared. There are significant differences between both the raw data (Fig. 9.25) and the PDFs (Fig. 9.26) between the ordered and disordered compounds as expected. As is clear from Eq. 3.39, in the PDF chemical ordering is manifest as changes in the peak intensities since the peak intensities are weighted by the atomic scattering factors of the pairs involved. This is evident in Fig. 9.26. Simple least-squares refinement using PDFFIT allowed the ordered and disordered compounds to be distinguished. However, a reverse Monte Carlo refinement of the data from the disordered material indicated that some short-range order persisted.

In the ordered sample, the CSRO parameters gave values exactly as expected for an ordered sample and persisted out indefinitely in r , as they should because the order is long ranged. In the case of the disordered sample, the CSRO parameters were not zero, the values for a random alloy, but deviated from zero in the sense that suggested that the same ordering scheme as seen in the ordered sample was persisting locally in the disordered sample. The nonzero CSRO parameters died out with increasing r and became insignificant around the sixth nearest neighbor. In this case, the residual order is probably the result of an imperfect quench rather than short-range order persisting above the ordering transition (the samples were quenched from 1200 K and the ordering transition is at 667 K). Nonetheless, it indicates that short-range order information can be extracted from the PDF. One thing that is apparent is that the signal of the CSRO in the PDF is rather weak. This is illustrated in Fig. 9.27 which shows the calculated PDF from the fully random model and that with the mild CSRO refined to

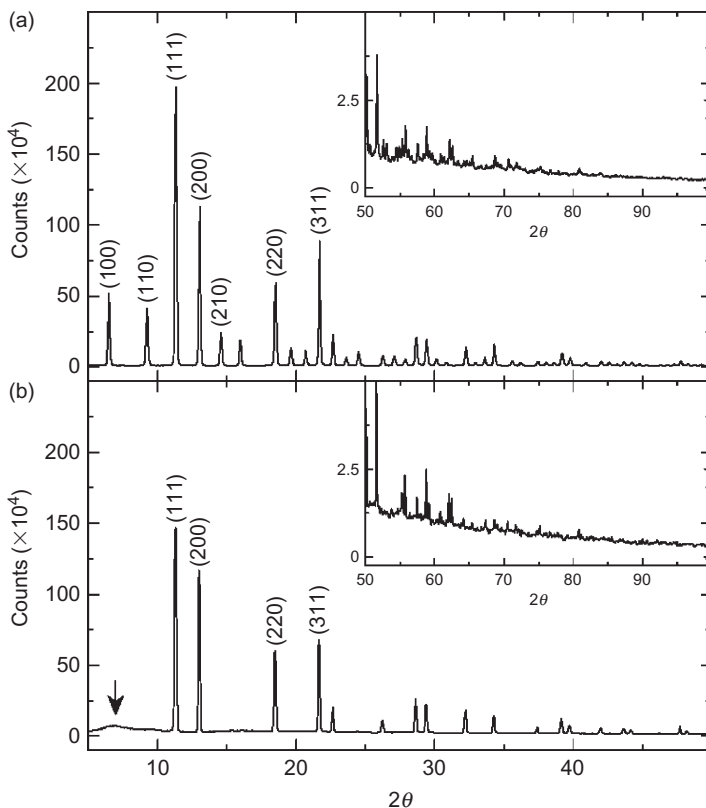


FIGURE 9.25 X-ray powder diffraction data from ordered (a) and disordered (b) samples of Cu_3Au . Superlattice peaks are clearly visible in the chemically ordered sample. Some diffuse scattering, presumably originating from CSRO is evident in the “disordered” sample below $2\theta = 10^\circ$ (Proffen *et al.*, 2002).

the disordered model. The difference curve, which has been multiplied by $3\times$, shows the difference that is rather small: obtaining high-quality data is especially important in these studies.

9.4. IN SITU AND IN OPERANDO STUDIES

9.4.1. *In Situ* RAPDF Studies of Chemical Reactions Under Flow

As mentioned above, the RAPDF technique is well suited for *in situ* measurements because of the highly penetrating high-energy X-ray beams that can get through environment cells and the transmission geometry with no moving parts. Basic environments such as low-temperature cryostats and high-temperature furnaces have been used in PDF experiments for a while, but more elaborate cells, such as reaction flow cells, are now becoming available

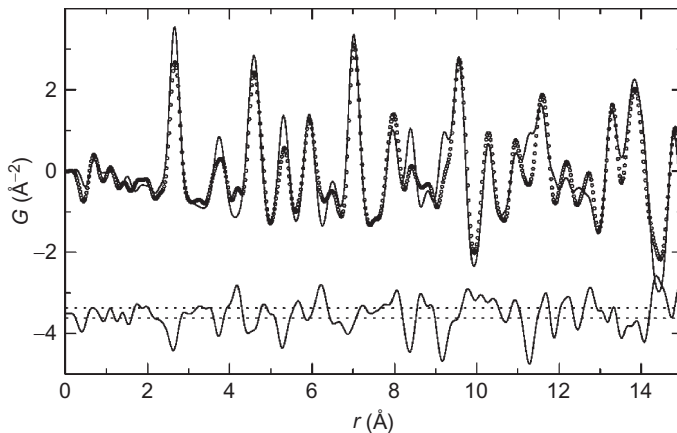


FIGURE 9.26 Experimental PDFs from disordered (circles) and ordered (solid line) Cu₃Au. The difference is given below as solid line. The estimated experimental uncertainty is marked by horizontal broken lines (Proffen *et al.*, 2002).

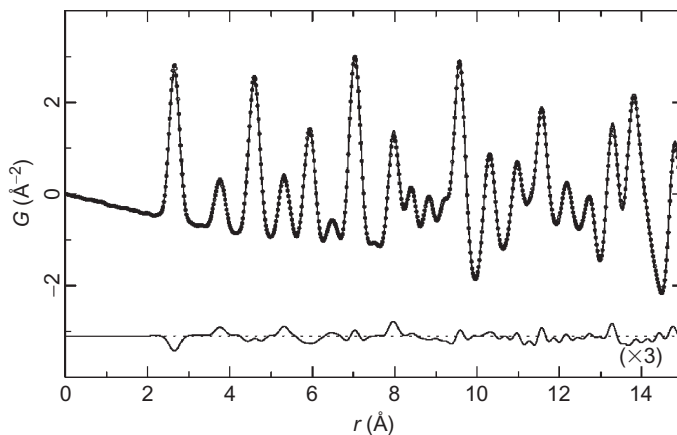


FIGURE 9.27 Calculated PDFs of the starting (solid line) and resulting structure (circles) of Cu₃Au from the RMC refinement that allows for chemical short-range order to exist in the “disordered” sample. The difference between both PDFs is enlarged by a factor of 3 and shown below the curves (Proffen *et al.*, 2002).

such as the one shown in Fig. 9.28 (Chupas *et al.*, 2008). These can be used for a wide variety of studies, for example, as discussed in Chupas *et al.* (2008), gas loading of porous materials (this is discussed in Section 10.4.1; Chapman *et al.*, 2006), high-temperature phase transition (i.e., using the device as a controlled atmosphere high-temperature furnace; Chupas *et al.*, 2004), controlled environment experiments, for example, in dry inert gas (Chapman *et al.*, 2006), and studying catalysts under operating conditions,

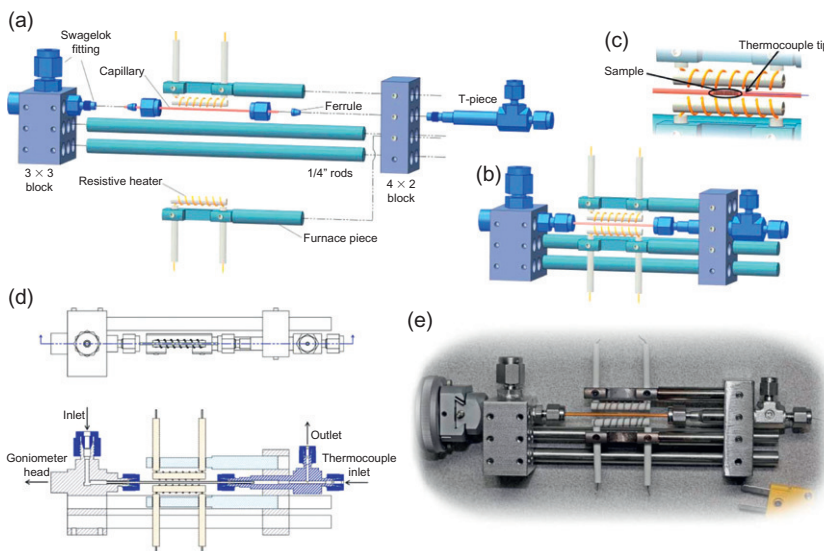


FIGURE 9.28 Exploded view of the flow cell for studying chemical reactions taking place under heat and flowing gases (Chupas *et al.*, 2008).

such as Au supported on ceria under water–gas-shift reaction conditions (Rodriguez *et al.*, 2007). RAPDF methods are ideal for studies of things such as nanoparticle growth on a support (Chupas *et al.*, 2007) which yields information about growth mechanisms.

This kind of *in situ* study is sure to grow in importance in the coming years as it reveals crucial information about physical processes that cannot be obtained in any other way.

9.4.2. PDF of an Operating Fuel Cell *In Operando*

The ultimate in *in situ* studies is *in operando* (the catalysis community sometimes calls this simply *operando*) in which an operating device is placed in the beam and studied as it operates. This could be a PDF study of the local structure of a battery electrode as the battery discharges, for example, or as in this work, a study of the Pt electrode catalysts in a fuel cell as it operates (Redmond *et al.*, 2012). One of the main failure mechanisms for proton exchange membrane fuel cells is loss of activity of the electrode catalyst, which is formed of Pt nanoparticles supported on a nanoporous carbon support. The mechanisms for this loss of activity are not fully understood but thought to include platinum loss and particle growth through (presumably) Ostwald ripening mechanisms. It is of the greatest interest to be able to study these effects in a real fuel cell under

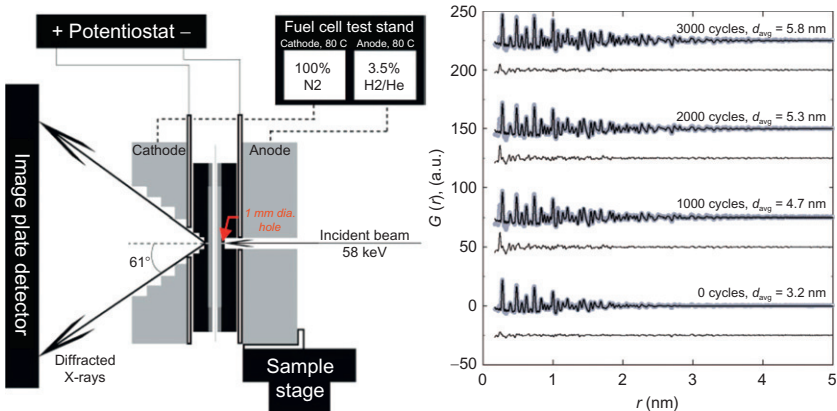


FIGURE 9.29 (left) Schematic diagram of the *in operando* fuel cell for use at a RAPDF beamline. Data were first measured with this device at 11IDB at APS. The resulting PDFs are shown in the right panel. The signal is coming predominantly from the Pt nanoparticles on the carbon support. It is clear that the signal extends to higher and higher r with the increasing number of fuel-cell cycles. Model fits are shown as the dark lines with the extracted NP size given in the figure and the difference curve offset below (Redmond *et al.*, 2012).

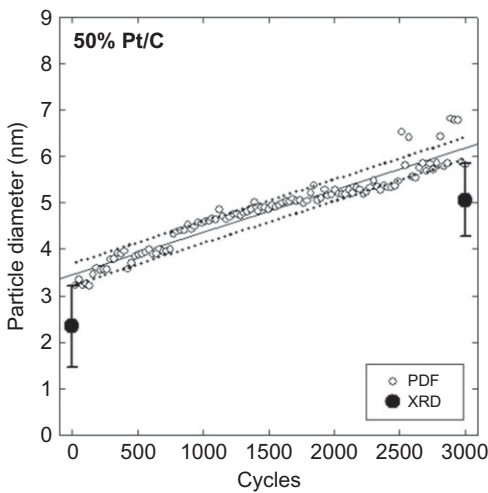


FIGURE 9.30 Diameter of the Pt nanoparticles extracted from PDF modeling as a function of number of fuel-cell cycles. The behavior is linear (or possibly sublinear) (Redmond *et al.*, 2012).

realistic conditions as it operates. As we discuss in Chapter 10, the PDF approach is ideal for the study of nanoparticle structure, and as discussed in Chapter 4, the RAPDF method ideal for *in situ* studies as implied here. The *in operando* fuel cell device for installation at a RAPDF beamline is shown in Fig. 9.29. The PDFs were measured in transmission using the RAPDF method

with a 58 keV beam. The resulting PDFs are shown in the same figure. It is clear directly by eye that the signal, which comes from the Pt nanoparticles, extends to higher- r with increasing number of fuel-cell cycles, clearly showing the nanoparticle growth. This can be quantified by fitting models that include the NP size, as described in Chapters 6 and 10. The dependence of the NP size on the number of fuel-cell cycles is shown in Fig. 9.30. The temperature dependence of the particle size growth appears linear or almost linear. Prior to the creation of the *in situ* cell, it was necessary to do the experiment destructively after a fixed number of cycles, and the temperature dependence could not be extracted in any meaningful way, but this becomes straightforward with an *in operando* device. The cycle dependence of the Pt catalysis degradation is an important parameter for physics models to understand the catalyst degradation and was only possible to measure in any kind of realistic fashion using an *in operando* method (Redmond *et al.*, 2012).

REFERENCES

- Acharya, M., Strano, M.S., Mathews, J.P., Billinge, S.J.L., Petkov, V., Subramoney, S. & Foley, H.C. (1999) *Philos. Mag. B*, **79**, 1499.
- Billinge, S.J.L. (2008) *J. Solid State Chem.*, **181**, 1698–1703.
- Billinge, S.J.L. & Kanatzidis, M.G. (2004) *Chem. Commun.*, 749–760.
- Billinge, S.J.L., DiFrancesco, R.G., Kwei, G.H., Neumeier, J.J. & Thompson, J.D. (1996) *Phys. Rev. Lett.*, **77**, 715–718.
- Bozin, E.S., Schmidt, M., DeConinck, A.J., Paglia, G., Mitchell, J.F., Chatterji, T., Radaelli, P.G., Proffen, Th. & Billinge, S.J.L. (2007) *Phys. Rev. Lett.*, **98**, 137203.
- Bozin, E.S., Malliakas, C.D., Souvatzis, P., Proffen, T., Spaldin, N.A., Kanatzidis, M.G. & Billinge, S.J.L. (2010) *Science*, **330**, 1660.
- Božin, E.S., Masadeh, A.S., Hor, Y.S., Mitchell, J.F. & Billinge, S.J.L. (2011) *Phys. Rev. Lett.*, **106**, 045501.
- Bozin, E.S., Juhas, P. & Billinge, S.J.L. (2012) C. Lamberti & G. Agostini (Eds.), *Characterization of Semiconductor Heterostructures and Nanostructures*. Amsterdam: Elsevier.
- Chapman, K.W., Chupas, P.J., Maxey, E. & Richardson, J.W. (2006) *Chem. Commun.*, **38**, 4013–4015.
- Cheetham, A.K., Fender, B.E.F. & Cooper, M.J. (1971) *J. Phys. C: Solid State Phys.*, **4**, 3107.
- Chupas, P.J., Chaudhuri, S., Hanson, J.C., Qiu, X., Lee, P.L., Shastri, S.D., Billinge, S.J.L. & Grey, C.P. (2004) *J. Am. Chem. Soc.*, **126**, 4756–4757.
- Chupas, P.J., Chapman, K.W., Jennings, G., Lee, P.L. & Grey, C.P. (2007) *J. Am. Chem. Soc.*, **129**, 4756–4757.
- Chupas, P.J., Chapman, K.W., Kurtz, C., Hanson, J.C., Leea, P.L. & Greyc, P.C. (2008) *J. Appl. Cryst.*, **41**, 822–824.
- Copley, J.R.D., Neumann, D.A., Cappelletti, R.L. & Kamitakahara, W.A. (1992) *J. Phys. Chem.*, **53**, 1353.
- Cowley, J.M. (1950) *J. Appl. Phys.*, **21**, 24.
- Cowley, J.M. (1995) *Diffraction Physics*. Amsterdam: Elsevier.
- Damay, P. & Leclercq, F. (1994) *Phys. Rev. B*, **49**, 7790.
- David, W.I.F., Ibberson, R.M., Matthewman, J.C., Prassides, K., Dennis, T.S.J., Hare, J.P., Kroto, H.W., Taylor, R. & Walton, D.M.R. (1991) *Nature*, **353**, 147.

- Dmowski, W., Contescu, C.I., Llobet, A., Gallego, N.C. & Egami, T. (2012) *J. Phys. Chem. C*, **116**, 2946.
- Dresselhaus, M.S., Dresselhaus, G. & Eklund, P.C. (1996) *Science of Fullerenes and Carbon Nanotubes*. New York: Academic Press.
- Drits, V.A., Sakharov, B.A., Salyn, A.L. & Manceau, A. (1993) *Clay Miner.*, **28**, 185–208.
- Egami, T., Dmowski, W. & Brezny, R. (1997) *SAE Publication 970461*; (1998) *SAE 1997 Trans.*, **106**, *J. Fuels Lubricants*, Sec. 4, 98.
- Franklin, R.E. (1950) *Acta Crystallogr.*, **3**, 107.
- Franklin, R.E. (1951) *Proc. R. Soc. Lond. A*, **209**, 196.
- Geim, A.K. & Novoselov, K.S. (2007) *Nat. Mater.*, **6**, 183–191.
- Grangeon, S., Lanson, B., Lanson, M. & Manceau, A. (2009) *Mineral. Mag.*, **72**, 1279.
- Heiney, P.A., Fischer, J.E., McGhie, A.R., Romanow, W.J., Denenstein, A.M., McAuley, J.P., Smith, A.B. & Cox, D.E. (1991) *Phys. Rev. Lett.*, **66**, 2911.
- Hiemstra, T. & Van Riemsdijk, W.H. (2009) *Geochim. Cosmochim. Acta*, **73**, 4423–4436.
- Hsu, K.F., Loo, S., Guo, F., Chen, W., Dyck, J.S., Uher, C., Hogan, T., Polychroniadis, E.K. & Kanatzidis, M.G. (2004) *Science*, **303**, 818.
- Hu, R.Z., Egami, T., Li, F. & Lannin, J.S. (1992) *Phys. Rev. B*, **45**, 9517.
- Hutchings, M.T., Clausen, K., Dickens, M.H., Hayes, W., Kjems, J.K., Schnabel, P.G. & Smith, C. (1984) *J. Phys. C: Solid State Phys.*, **17**, 3903.
- Janney, D.E., Cowley, J.M. & Buseck, P.R. (2000) *Am. Mineral.*, **85**, 1180–1187.
- Jensen, K.M.O., Bozin, E.S., Malliakas, C.D., Stone, M.B., Lumsden, M.D., Kanatzidis, M.G., Shapiro, S.M. & Billinge, S.J.L. (2012) *Phys. Rev. B*, **86**, 085313.
- Juhás, P., Cherba, D.M., Duxbury, P.M., Punch, W.F. & Billinge, S.J.L. (2006) *Nature*, **440**, 655.
- Keen, D.A. (2002) *J. Phys. Condens. Matter*, **14**, R819.
- Kim, H.J., Bozin, E.S., Haile, S.M., Snyder, G.J. & Billinge, S.J.L. (2007) *Phys. Rev. B*, **75**, 134103.
- Krivoglaz, M.A. (1969) *Theory of X-ray and Thermal-Neutron Scattering by Real Crystals*. New York: Plenum.
- Krivoglaz, M.A. (1996) *Diffuse Scattering of X-rays and Neutrons by Fluctuations*. Berlin: Springer.
- Leclercq, F., Damay, P., Foukani, M., Chieux, P., Bellissent-Funel, M.C., Rassat, A. & Fabre, C. (1993) *Phys. Rev. B*, **48**, 2748.
- Leyssale, J.M., Da Costa, J.P., Germain, C., Weisbecker, P. & Vignoles, P. (2009) *Appl. Phys. Lett.*, **95**, 231912.
- Li, F., Ramage, D., Lannin, J.S. & Conceicao, J. (1991) *Phys. Rev. B*, **44**, 13167.
- Lin, H., Bozin, E.S., Billinge, S.J.L., Androulakis, J., Lin, C.H. & Kanatzidis, M.G. (2009) *Phys. Rev. B*, **80**, 045204.
- Lin, H., Bozin, E.S., Billinge, S.J.L., Quarez, E. & Kanatzidis, M.G. (2005) *Phys. Rev. B*, **72**, 174113.
- Malavasi, L., Billinge, S.J.L., Kim, H.J., Proffen, Th., Tealdi, C. & Flor, G. (2007) *J. Am. Chem. Soc.*, **129**, 6903.
- Malavasi, L., Kim, H.J. & Proffen, T. (2009) *J. Appl. Phys.*, **105**, 123519.
- Mamontov, E. & Egami, T. (2000) *J. Phys. Chem. Solids*, **61**, 1345.
- Mamontov, E., Egami, T., Brezny, R., Koranne, M., Juskelis, M. & Tyagi, S. (2000) *J. Phys. Chem. B*, **104**, 11110.
- Manceau, A. (2009) *Clay Miner.*, **44**, 19–34.
- Manceau, A. (2010) *Clay Miner.*, **45**, 225–228.
- Michel, F.M., Ehm, L., Antao, S.M., Lee, P.L., Chupas, P.J., Liu, G., Strongin, D.R., Schoonen, M.A.A., Philips, B.L. & Parise, J.B. (2007) *Science*, **316**, 1726.

- Michel, F. M., Hosein, H.A., Hausner, D.B., Debnath, S., Parise, J.B., Strongin, D.R., *Biochimica et Biophysica Acta*, **1800**, 871.
- Moss, S.C. (1964) *J. Appl. Phys.*, **35**, 3547.
- Nield, V.M. & Keen, D.A. (2001) *Diffuse Neutron Scattering from Crystalline Materials*. Oxford: Oxford Science Publications.
- Paglia, G., Bozin, E.S. & Billinge, S.J.L. (2006) *Chem. Mater.*, **18**, 3242.
- Petkov, V., DiFrancesco, R.G., Billinge, S.J.L., Acharya, M. & Foley, H.C. (1999) *Philos. Mag. B*, **79**, 1519.
- Petkov, V., Ren, Y., Saratovsky, I., Pasten, P., Gurr, S.J., Hayward, M.A., Poeppelmeier, K.R. & Gaillard, J.-F. (2009) *ACS Nano*, **3**, 441.
- Pintschovius, L. (1998) *Phase Transit.*, **67**, 295.
- Proffen, T. (2000) *Z. Kristallogr.*, **215**, 661.
- Proffen, T., Petkov, V., Billinge, S.J.L. & Vogt, T. (2002) *Z. Kristallogr.*, **217**, 47.
- Radaelli, P.G., Horibe, Y., Gutmann, M.J., Ishibashi, H., Chen, C.H., Ibberson, R.M., Koyama, Y., Hor, Y.S., Kiryukhin, V. & Cheong, S.W. (2002) *Nature*, **416**, 155.
- Rancourt, D.G. & Meunier, J.F. (2008) *Am. Mineral.*, **93**, 1412.
- Redmond, E.L., Setzler, B.P., Juhas, P., Billinge, S.J.L. & Fuller, T.F. (2012) *Electrochem. Solid State*, **15**, B72.
- Rodriguez, J.A., Wang, X., Liu, P., Wen, W., Hanson, J.C., Hrbek, J., Perez, M. & Evans, J. (2007) *Top. Catal.*, **44**, 73.
- Saito, R., Dresselhaus, M.S. & Dresselhaus, G. (1998) *Physical Properties of Carbon Nanotubes*. London: Imperial College Press.
- Sartbaeva, A., Wells, S.A., Thorpe, M.F., Bozin, E.S. & Billinge, S.J.L. (2007) *Phys. Rev. Lett.*, **99**, 155503.
- Soper, A.K., David, W.I.F., Sivia, D.S., Dennis, T.J.S., Hare, P. & Prassides, K. (1992) *J. Phys. Condens. Matter*, **4**, 6087.
- Thorpe, M.F., Levashov, V.A., Lei, M. & Billinge, S.J.L. (2002) S.J.L. Billinge & M.F. Thorpe (Eds.), *From Semiconductors to Proteins: Beyond the Average Structure* (p. 105). New York: Kluwer/Plenum.
- Warren, B.E. (1934) *J. Chem. Phys.*, **2**, 551.
- Warren, B.E. (1941) *Phys. Rev.*, **9**, 693.
- Warren, B.E. (1990) *X-ray Diffraction*. New York: Dover.
- Weisbecker, P., Leyssale, J.M., Fischer, H.E., Honkimaki, V., Lalanne, M. & Vignoles, G.L. (2012) *Carbon*, **50**, 1563.
- Young, C.A. & Goodwin, A.L. (2011) *J. Mater. Chem.*, **21**, 6464.
- Zhang, Y.B., Tan, Y.W., Stormer, H.L. & Kim, P. (2005) *Nature*, **438**, 201.
- Zhu, M.Q., Ginder-Vogel, M., Parikh, S.J., Feng, X.H. & Sparks, D.L. (2010) *Environ. Sci. Technol.*, **44**, 4465.